Comparison of continuous-wave CO_2 lidar calibration by use of Earth-surface targets in laboratory and airborne measurements

Maurice A. Jarzembski and Vandana Srivastava

Backscatter of several Earth surfaces was characterized in the laboratory as a function of incidence angle with a focused continuous-wave 9.1-μm CO_2 Doppler lidar for use as possible calibration targets. Some targets showed negligible angular dependence, while others showed a slight increase with decreasing angle. The Earth-surface signal measured over the complex Californian terrain during a 1995 NASA airborne mission compared well with laboratory data. Distributions of the Earth's surface signal shows that the lidar efficiency can be estimated with a fair degree of accuracy, preferably with uniform Earth-surface targets during flight for airborne or space-based lidar.

OCIS codes: 010.3640, 280.3640, 290.1350.

1. Introduction

Airborne lidar systems are being used to determine wind velocity[1] and to measure aerosol- or cloud-backscatter variability with high resolution over large spatial scales.[2–4] While these measurements are made, the lidar also often retrieves a distinct backscatter signal from the Earth's surface.[1] Unlike atmospheric backscatter, which is highly variable both spatially and temporally, Earth-surface backscatter is relatively much less variant and can be quite predictable. Therefore routine backscatter measurements by an airborne or space-based lidar from designated Earth surfaces with known and fairly uniform backscatter properties can potentially offer lidar calibration opportunities. This calibration can in turn be used to obtain accurate atmospheric aerosol- and cloud-backscatter measurements on large spatial scales. Earth-surface backscatter is important, because achieving a precise calibration factor for large pulsed lidars then need not rest solely on use of a standard hard target (HT) procedure, which can be quite exhaustive and costly. Furthermore, calibration from designated Earth surfaces would provide an in-flight performance evaluation of the lidar for monitoring misalignments or laser–detector degradation. The potential uncertainty in a calibration factor obtained with a standard HT before field measurements may be comparable with or even higher than when several designated Earth surfaces with well-defined backscatter properties encountered during field measurements are used. Already, many passive remote-sensing-satellite instruments are encountering and analyzing Earth surface scattering at different wavelengths; e.g., the advanced very high resolution radiometer (AVHRR) uses ocean- and desert-surface scattering to calibrate its instrument occasionally.[5] Hence, with active remote sensing with lasers that have high-resolution data, calibration of a space-based lidar[6,7] by use of the Earth surfaces will be extremely useful.

The calibration methodology with the Earth's surface initially requires measuring backscatter of various Earth surfaces simulated in the laboratory and the use of these backscatter measurements as standards for the Earth-surface signal from airborne or space-based lidars. Since backscatter from the Earth's surface may be retrieved at different angles of incidence, this work presents measured backscatter at various angles of incidence of different simulated Earth-type surfaces in the laboratory with a focused continuous wave (cw) CO_2 Doppler lidar at a 9.1-μm wavelength. In general, Earth-surface reflectance

M. A. Jarzembski is with the Global Hydrology and Climate Center, NASA Marshall Space Flight Center, 977 Explorer Boulevard, Huntsville, Alabama 35806. His email address is maurice.jarzembski@msfc.nasa.gov. V. Srivastava is with the Global Hydrology and Climate Center, Institute for Global Change Research and Education, Universities Space Research Association, 977 Explorer Boulevard, Huntsville, Alabama 35806. His email address is vandana.srivastava@msfc.nasa.gov.

Received 1 October 1997; revised manuscript received 18 June 1998.

measurements have been made in the infrared,[8] but the use of lidars to characterize them and in turn use of the Earth's surface to calibrate lidars has not been made. The feasibility of this calibration methodology is demonstrated through a comparison of these laboratory measurements with actual Earth-surface backscatter retrieved from the same lidar during the NASA/Multi-center Airborne Coherent Atmospheric Wind Sensor (MACAWS) mission[1] on NASA's DC8 aircraft from 13–26 September 1995. For selected Earth-surface scenarios from the airborne lidar data, an average backscatter for the surface was established and the statistics of lidar efficiency with these selected surfaces was determined. These data were compared with the actual lidar efficiency determined with the standard calibrating hard target (CHT). This methodology can be carried out for other lidar wavelengths.

2. Lidar Theory

The measured signal-to-noise ratio (SNR) from a HT surface with backscatter ρ_{HT} (sr^{-1}) (reflected power per steradian toward the receiver, divided by the incident power) with a cw lidar is given by the general expression[9,10]

$$\mathrm{SNR}_{HT} = \eta_{HT} K_{HT} T \rho_{HT}, \tag{1}$$

where η is the overall lidar system efficiency and K is a proportionality factor that depends on several directly measurable lidar parameters. The transmission efficiency T is given by $T = \exp(-2\alpha L)$, where α is the atmospheric attenuation coefficient at the lidar wavelength over the path L to the scattering target.[11] At close distances (e.g., in the laboratory), T is unity; however, at long distances it decreases and needs to be taken into account. HT can stand for a standard CHT or earth hard target (EHT), since both present a surface of scattering. Equation (1) is used with a CHT, such as flame-sprayed aluminum (FSA) or sandpaper (SND), with known ρ_{CHT} to determine η_{CHT}.

For a distance L from a focused cw-lidar primary mirror to the HT surface, K_{HT} is given by[10,12]

$$K_{HT} = P\pi R^2 f(L)/Bh\nu, \tag{2}$$

where range dependence $f(L)$ is given by

$$f(L) = 1/\{L^2[1 + (\pi R^2/\lambda L)^2(1 - L/F)^2]\}, \tag{3}$$

where $h\nu$ is the laser photon energy, P is the transmitted laser power, R is the lidar-beam $(1/e)^2$ intensity radius at the telescope primary mirror, F is the distance to the center of the focal volume, and B is the data-system bandwidth. At the lidar-beam focal volume $L = F$, Eqs. (1)–(3) reduce to

$$\mathrm{SNR}_{HT} = \eta_{HT} P\pi R^2 T \rho_{HT}/Bh\nu F^2. \tag{4}$$

By use of a CHT with known ρ_{CHT}, as other lidar parameters are measurable, η_{CHT} can be determined.[12] This can be done either with Eqs. (1)–(3) and measurement of SNR_{CHT} at various distances L or with Eq. (4) and measurement of SNR_{CHT} only at the focal volume. Once η_{CHT} is known then measured SNR_{HT} from any other HT surface can lead to ρ_{HT} by inversion of either Eqs. (1)–(3) or Eq. (4). Thus ρ_{EHT} for a variety of Earth-surface compositions can be characterized in the laboratory. Subsequently, the characterized Earth surfaces can be used as calibration targets in flight to obtain η_{EHT} for airborne or space-based lidars. Finally, once η_{EHT} has been determined, then it may be further corrected to $\eta_{AEROSOL}$, the lidar efficiency determined with laboratory-generated aerosols, which results in a more realistic assessment of the actual lidar efficiency to be used for atmospheric measurements.[12]

3. Laboratory Experiment and Airborne Mission

The NASA/Marshall Space Flight Center's (MSFC's) focused cw 9.1-μm CO_2 Doppler lidar was used for measuring backscatter. Details of the lidar operation and its calibration procedure can be found elsewhere.[12,13] Laboratory simulation was conducted with a variety of homogeneous HT's made from Earth-surface materials. SNR_{HT} was measured with a spectrum analyzer (SA) as a function of incidence angle φ (the angle between the lidar beam meeting the surface and normal to the surface) at the focal volume. Different targets were investigated to provide an envelope of a variety of materials that may be found in Earth surfaces, homogeneous (e.g., sand, soil, snow, water, and single-type vegetation) as well as heterogeneous (e.g., vegetation interspersed with open land and cities). During the 1995 NASA/MACAWS mission, while atmospheric aerosol backscatter was being detected, SNR_{EHT} was also measured during aircraft rolls at different ranges for various Earth surfaces with diverse compositions from nearly homogenous to quite heterogeneous mixtures. These measurements of SNR_{EHT} were corrected for atmospheric attenuation and compared with theoretical SNR_{EHT} by use of the ρ_{EHT} from simulated Earth surfaces measured in the laboratory. From this comparison, the statistics of η_{EHT} for selected Earth surfaces having an average ρ_{EHT} was determined and compared with the measured lidar efficiency by use of the SNL CHT.

A. Backscatter from Simulated Earth Surfaces

Figure 1 shows an experimental arrangement for backscatter measurements of simulated Earth-type (a) land surfaces and (b) wet surfaces. Numerous materials were used to simulate land-surface HT's: oak, pine, corn, sand, soil, and roof tar. The material was glued, with rubber cement, onto 8-in-diameter plexiglass disks. For the vegetation targets, vegetation was cut into small pieces with sizes of roughly several millimeters. The HT was attached to a rotating motor shaft to give a Doppler-frequency-shifted signal. It could be moved along an optical rail to give range response of $\mathrm{SNR}(L)$, or it could be placed at the center of the lidar-beam focal volume for range $L = F$ [Fig. 1(a)]. Here φ was

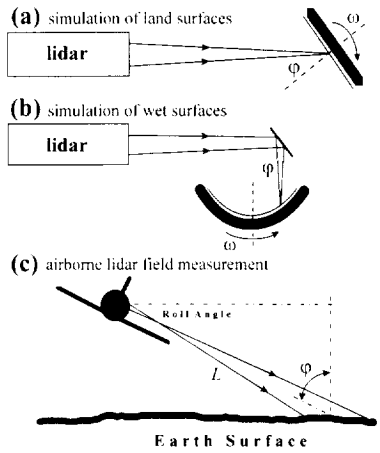

Fig. 1. Laboratory schematic for backscatter measurement of simulated Earth-type (a) land surfaces and (b) wet surfaces. Airborne measurement scenario (c) of retrieval of an Earth-surface backscatter signal from the expanded cw-lidar beam during an aircraft roll.

changed by the turning of the HT with respect to the lidar-beam axis.

Simulations of wet surfaces were performed in a different experimental setup [Fig. 1(b)]. A rotating vessel containing the wet material, placed on a motor shaft, produced a smooth parabolic surface, owing to centrifugal force. The equation of the curve in two dimensions was geometrically determined to be $z \sim 0.13r^2$ at a constant angular speed. With the lidar beam directed at different spots on the parabolic water surface, different φ could be accurately determined by use of the vector calculus equation $\varphi = \cos^{-1}(\mathbf{N} \cdot \mathbf{I}/|\mathbf{N}||\mathbf{I}|)$, where $\mathbf{I}$ is the incident lidar-beam vector and $\mathbf{N}$ is the surface normal vector, which were geometrically measured. Other targets, such as melted snow simulating the Earth's ice-capped–snow regions and soapy water simulating a choppy-ocean-water surface with white caps, were also investigated.

With Eqs. (1)–(3), η_{CHT} was determined from the measured $SNR_{CHT}(L)$ of two CHT's, (SND and FSA), and their ρ_{CHT} at $\varphi = 45°$ is given by 7.33×10^{-3} sr^{-1} and 8.28×10^{-2} sr^{-1}, respectively, with ~4% uncertainty.[14,15] Other lidar parameter values were $h\nu = 2.1818 \times 10^{-20}$ J, $P = 2.9$ W ± 1%, $R = 0.0305$ m ± 1.5%, $F = 9.33$ m ± 0.5%, and $B_{SA} = 360$ kHz ± 1%. The uncertainty in measuring SNR in the laboratory with SA was ~7%. The CHT's gave $\eta_{SND} \sim 0.17 \pm 9\%$ and $\eta_{FSA} \sim 0.16 \pm 9\%$. An average value of $\eta_{CHT} \sim 0.165 \pm 13\%$ was used as the lidar system efficiency for determining the backscatter of various simulated EHT surfaces.

For the various land and wet Earth-surface simulations, SNR_{EHT} was measured as a function of φ at $L = F$. Then, from Eq. (4), ρ_{EHT} was determined with the previously mentioned lidar parameter values. Figure 2 shows ρ_{EHT} as a function of φ for (a) land-type targets and (b) wet-type targets. Uncertainty in ρ_{EHT} for land-type targets is ~12%, while for

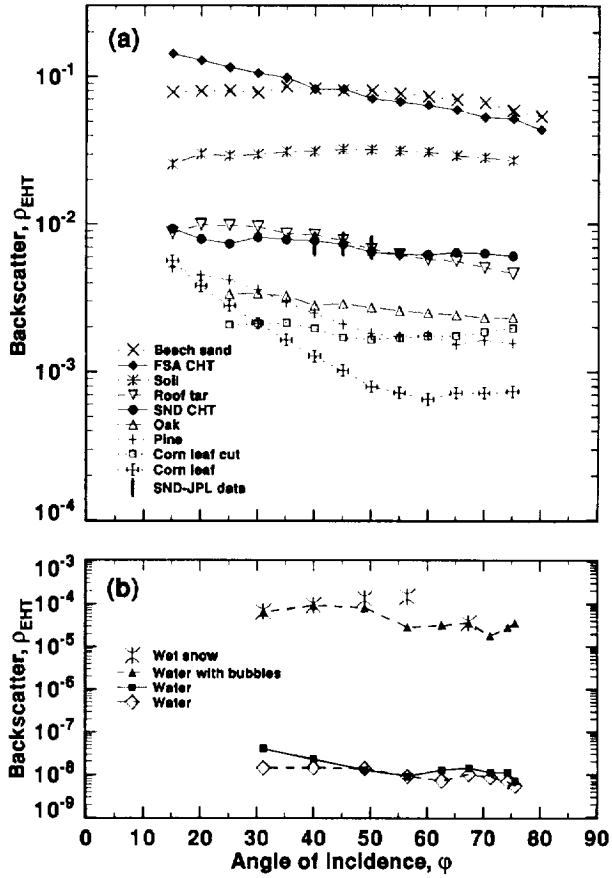

Fig. 2. Laboratory backscatter measurements as a function of angle of incidence φ with the NASA/MSFC 9.1-μm cw Doppler lidar from simulated Earth surfaces for (a) land-type targets and (b) wet-type targets.

the wet-type targets, the uncertainty is higher. In general, for all the simulated EHT land-type surfaces, dependence of ρ_{EHT} on φ is small. Some of the surfaces, such as FSA, pine needles, and uncut corn leaves, show an increase in ρ_{EHT} for smaller φ; whereas others, such as SND, beach sand, soil, roof tar, oak, and cut corn leaves, show almost no φ dependence. These results show that there are several naturally occurring targets that behave like the standard FSA and SND CHT's and can provide reasonable calibrating targets during flight. For the land-type simulated EHT surfaces, sand and soil targets give the highest ρ_{EHT}, while vegetation targets give the lowest. Additionally, the vegetation targets that were dried out had negligible change on ρ_{EHT}. However, wetting all targets with water lowered the ρ_{EHT} dramatically for all φ. This follows the same trend with the wavelength-dependent reflectance measurement of dry and wet terrestrial surfaces in the near infrared,[8] thus showing that wet targets had lower reflectance. However, backscatter measurements of wetted targets could not be accurately quantified as a function of water content for this experiment, because the amount of water changed rapidly in time, owing to the HT angular rotation.

For the wet surfaces [Fig. 2(b)], smooth water had

the lowest ρ_{EHT} of all HT's. This supports the previous observation that the presence of water ($\rho_{EHT} \sim 10^{-8}$ sr^{-1}) on wetted land-type targets lowered ρ_{EHT} as compared with dried targets ($\sim 10^{-3}$–10^{-1} sr^{-1}). The presence of small ripples on the smooth water surface tended to increase the ρ_{EHT} of water. As the ripples became larger, ρ_{EHT} also increased. Furthermore, the addition of soap bubbles to the smooth water surface greatly enhanced water ρ_{EHT} by more than 3 orders of magnitude. High backscatter was also measured for snow. Despite the drastic dissimilarity between snow and soap bubbles on the water surface, ρ_{EHT} for both were nearly the same. Even though refractive indices of water and ice are similar at the 9.1-μm wavelength, backscatter appears to be affected solely by the surface-shape irregularities of snow, which shows a dramatic difference between low signals from smooth water surfaces and high signals from irregular surfaces. Also, the addition of soil to either soap bubbles or snow tended to further increase ρ_{EHT}, which again agrees with the finding that the ρ_{EHT} of soils ($\sim 10^{-1}$ sr^{-1}) was found to be higher than that of snow or of water with soap bubbles (10^{-5}–10^{-4} sr^{-1}).

The investigated targets gave a range of possible variation in the ρ_{EHT} that may be encountered during field missions from real Earth surfaces composed of different materials. Figure 2 shows that for the simulated land-type Earth surfaces, backscatter at 9.1 μm varies by a factor of ~50, depending on whether the simulated Earth surface is purely vegetation type or purely nonvegetation type, or a mixture of the two. For mixed surfaces, if the fractions of different materials can be estimated, then an average ρ_{EHT} can be estimated by weighted mixing of their individual ρ_{EHT}'s. With the use of passive satellite imagery, such as LANDSAT, it may be possible to fractionate different types of surfaces encountered in the lidar-sampled surface area. For calibration purposes, homogeneous surfaces would be best; but if these were not available, than an average ρ_{EHT} of a composite surface could be used.

The measurements shown in Fig. 2 were made at the lidar-beam focus. However, backscatter measurements made from actual Earth surfaces with an airborne-focused cw lidar are performed at random range values, depending on the aircraft altitude and roll. Therefore measurements of the range response of backscatter from the simulated Earth surfaces were performed in the laboratory to show that the measurements followed the same behavior as the theory predicted [Eqs. (1)–(3)] and hence to support the possibility that the η_{EHT} may be determined from SNR_{EHT} at any range for these targets. Figure 3 shows the range response of HT made from beach sand and pine, as well as the SND CHT. The beach sand and pine HT's show good agreement with lidar theory, which is similar to the case of SND CHT.[12] The range response of backscatter for the other land-type HT's (not shown in Fig. 3) also were in good agreement with the lidar theory. These results suggest that the signal from these types of Earth surfaces at ranges other than $L = F$ can be used in conjunction with Eqs. (1)–(3) to estimate lidar efficiency.

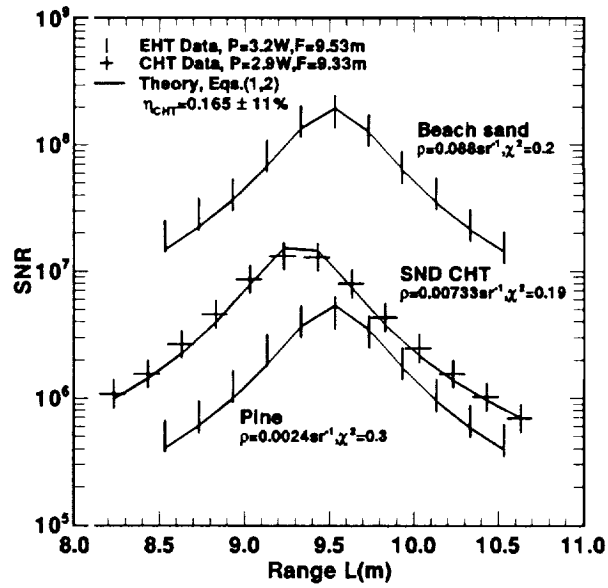

Fig. 3. Measured backscattered SNR as a function of range L for beach sand and pine HT's and the (SND) calibrating HT.

B. Earth-Surface Return

Figure 1(c) shows a schematic of how the NASA/MSFC airborne cw-focused 9.1-μm lidar retrieved an Earth-surface backscatter at the unfocused part of the lidar beam along with atmospheric aerosol backscatter at the lidar-beam focus during an aircraft roll for the MACAWS mission. The lidar beam was focused at ~54 m through a modified aircraft right-side-viewing germanium window in front of the aircraft wing. Usually, it is not overly difficult to distinguish backscatter between aerosols and the Earth's surface. As the aircraft entered a roll, a small Earth-surface signal emerged at a distance L. As the roll angle increased, φ decreased, which decreased L; the mean signal strength increased, according to Eqs. (1)–(3), and the signal could be easily followed for the duration of the roll. Usually this signal had a Doppler-frequency shift lesser or greater than that of the aerosol signal, and therefore a separate SNR for each signal could be retrieved. On occasion the two signals overlapped, and a separate SNR for both aerosol and the Earth's surface could not be obtained. Generally, the Earth-surface signal tended to have a narrower spread in frequency than the aerosol signal, which has an additional spread, owing to turbulence.

Figure 4 shows both the aerosol signal and the Earth-surface signal from the focused cw lidar during an aircraft roll, as displayed on the digital signal processor in real time for 1 s of integration. The Earth-surface signal was from the expanded lidar beam and was from agricultural land located in the Sacramento Valley near Willows, California. With

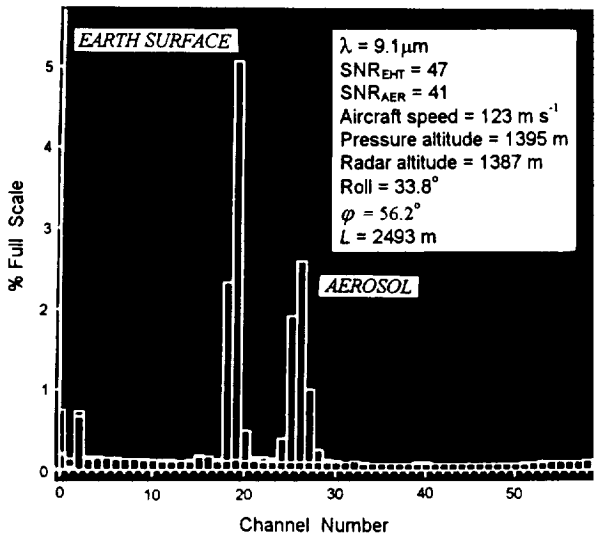

Fig. 4. 1-s integrated cw-lidar spectral data taken with the digital signal processor of both an aerosol and an Earth-surface land backscatter signal at different Doppler-shift frequencies during an aircraft roll over Sacramento Valley near Willows, California, located at approximately 39° 25′ N. lat, 122° 15′ W. long.

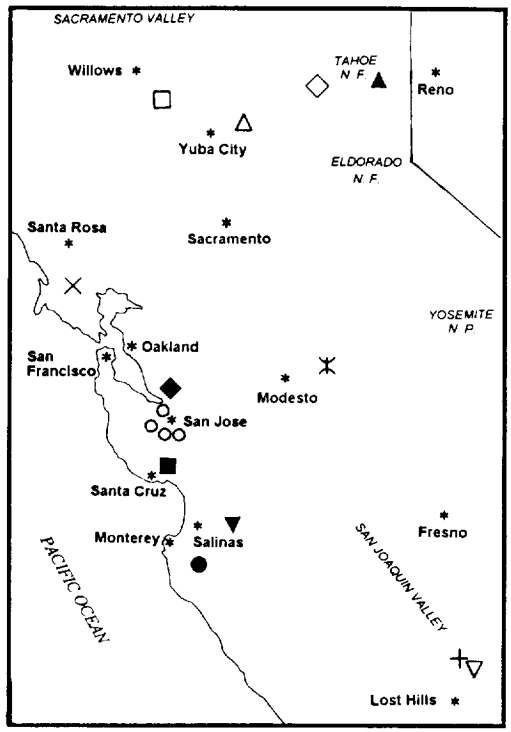

Fig. 5. Map of region of California showing the locations where different Earth-surface measurements were made as illustrated by different symbols.

propagation of a Gaussian lidar beam, the lidar-beam cross-sectional area near the surface was ~6.4 m^2 with a projected area of ~11.6 m^2 along the surface. For the DC8 aircraft speed of ~123 m s^{-1}, this corresponds to Earth-surface sampling of approximately 123-m long × ~5.2 m wide, or approximately 0.15 acres s^{-1}. In contrast, aerosol backscatter was within the lidar focal volume with a beam cross-sectional area of ~8 × 10^{-5} m^2 and an integrated sample volume of approximately 65 m^3. Despite drastic dissimilarities in beam sizes and intensities at the focal volume for aerosols and at the expanded beam at the Earth's surface, strength in signal from aerosols and from the Earth's surface can be comparable. This is due to the relatively weak aerosol backscatter at the high-intensity part of the lidar beam and the relatively strong Earth-surface backscatter at the low-intensity part of the lidar beam for $L \gg F$ (as shown in Fig. 6 of Ref. 12).

The outgoing lidar beam to the Earth's surface and the backscatter from the surface can undergo appreciable atmospheric attenuation.[11] The retrieved SNR from the Earth's surface needs to be compensated for attenuation. The significant factors are given in terms of the attenuation coefficient α of major atmospheric components: aerosol (α = 0.024 km^{-1}), carbon dioxide (CO_2 line, α = 0.0014 km^{-1}), and water (H_2O line, α = 0.0064 km^{-1} and H_2O continuum, α = 0.05 km^{-1}). The average values for CO_2 and H_2O absorption lines were derived from line-by-line computations[16] while the H_2O continuum was derived from LOWTRAN 7 with representative meteorological conditions for the California area.[17] The average aerosol α value was derived from the integrated aerosol backscatter with measured vertical profiles obtained from ascents and descents during the MACAWS mission. The total transmission efficiency T, which typically ranged from 55% to 75%, was estimated for each datum with the aircraft radar altitude and roll angle.

The geographical location of the various regions where a backscatter signal from the Earth's surface was obtained during an aircraft roll are shown Fig. 5. Different surfaces encountered were vegetation and nonvegetation agricultural areas over California's San Joaquin (open inverted triangle, plus, and ant) and Sacramento (open square) Valleys; forest mixed with sparse open land over the Sierra Nevada Mountains west of Reno, Nevada (filled triangle, open diamond, and open triangle), and over the Coastal Range Mountains in California near Monterey (filled circle), Santa Cruz (filled square), Salinas (filled inverted triangle), and Santa Rosa (cross); and grassland east of San Francisco Bay (filled diamond) and metropolitan areas in the South Bay area (open circle). Although the DC8 made many rolls over the open ocean, no signal from a relatively calm ocean surface (even at L ~ 500 m) could be detected with the given output power of the lidar. This was probably due to the water's low backscatter (Fig. 2).

Figure 6 shows measured SNR normalized by T (SNR_{EHT} = SNR/T) at various ranges from the Earth-surface locations identified by the symbols shown in Fig. 5. Each data point represents averaging over several 1-s samples, ranging from 7 to 53 samples. The horizontal line through each data point gives the L variability that is due to both roll angle and radar altitude, whereas the vertical line

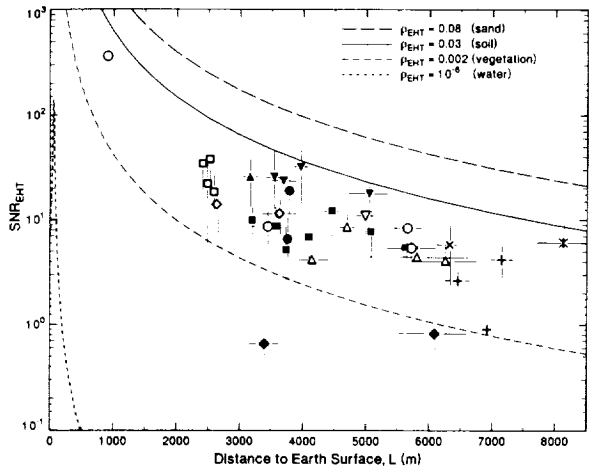

Fig. 6. Measured backscattered SNR normalized by transmission efficiency T for the various Earth surfaces shown in Fig. 5 with the 9.1-μm cw lidar along with comparison with lidar theory [Eqs. (1)–(3)] by use of lidar parameters cited in the text for four representative backscatter values of various Earth-surface types. Variability of Earth-surface backscatter at each location is depicted by the vertical line through each data point, which gives the range of SNR_{EHT} at a given distance, while variability in L is depicted by the horizontal line through each data point, which gives the range of L that is due to variability in both radar altitude and roll angle.

gives SNR_{EHT} variability over the sampled surface. For some samples, SNR_{EHT} was relatively constant, e.g., grass hills interspersed with some trees and shrubs (filled diamond) and also for metropolitan areas (open circle) which, even though inhomogeneous, form a uniform mixture without significant backscatter changes between consecutive samples. Whereas for other regions, such as over the valley and coastal ranges, there is more variability of SNR_{EHT}, caused by significant heterogeneity encountered as a result of low-backscatter vegetation interspersed with high-backscatter nonvegetation areas. Figure 6 also shows curves of predicted SNR_{EHT} as a function of L with Eqs. (1)–(3) for four Earth-surface types simulated in the laboratory with ρ_{EHT} = 0.08, 0.03, 0.002, and 10^{-6} sr^{-1} (Fig. 2) corresponding to sand, soil, vegetation, and water with ripples, respectively. These curves were derived with the various lidar parameter values during the mission as $h\nu = 2.1818 \times 10^{-20}$ J, P = 4.4 W ± 3%, R = 0.0265 m ± 3%, F = 54.0 m ± 2%, and B_{DSP} = 141 kHz ± 1% during the MACAWS mission. The measurement error in the SNR on the airplane during calibration with the SND CHT was ~8%. The uncertainties given here for the mission and those given earlier for the lab measurements represent instrument-related errors. The average lidar efficiency as measured at the beam focus during several calibration measurements performed for this two-week mission period with the SND CHT was $\eta_{CHT} \sim 0.126 \pm 18\%$.

Most of the data were bounded between soil and vegetation and follow the trend of decreasing SNR_{EHT} with increasing L, as predicted by theory. For the metropolitan areas (open circle), which would be composed mostly of high-backscatter targets such as concrete-type materials, roof tar, metals, soils mixed with low-backscatter targets such as vegetation, ρ_{EHT} was bounded by the curves of soil and vegetation. The grass hills interspersed with trees and shrubs (filled diamond) east of the Bay area gave low SNR_{EHT}, close to that predicted for vegetation. In this case the long grass offers a good ground cover over soil, so backscatter from soil was not expected. Forested areas interspersed with open land in the Sierra Nevada Mountains (filled triangle, open diamond, and open triangle) and the Coastal Range Mountains (cross, filled square, filled circle, and filled inverted triangle) gave an SNR_{EHT} between soil and vegetation values; however, near Salinas (filled inverted triangle), more sparse vegetation on the eastern slopes showed the highest SNR_{EHT}. Furthermore, SNR_{EHT} from Sacramento (open square) and San Joaquin (open inverted triangle, plus, and ant) Valleys each showed that the targets were heterogeneous, mixed with vegetation and nonvegetation types.

The sand, soil, and vegetation targets, even though they were made from Alabama sources, provide a good envelope of possible SNR_{EHT} from surfaces that may contain similar materials. To get a one-to-one agreement between heterogeneous surfaces sampled during the flight with theoretical predictions, actual Earth-surface samples encountered in the mission would be needed to determine their ρ_{EHT} in the laboratory. The measured SNR_{EHT} from a 9.1-μm lidar for different Earth surfaces encountered here ranged within a factor of ~50, as is also seen from lab measurements in Fig. 2.

Some comparison can be made with the Earth-surface signal obtained during the follow-on 1996 MACAWS mission[1] by the calibrated 10.6-μm pulsed lidar. Lab characterization of ρ_{CHT} from 9.1- to 10.6-μm wavelengths shows similar values.[14] The ρ_{EHT}, at 10.6 μm, retrieved over San Joaquin Valley ranged from ~0.003 to 0.031 sr^{-1}, encompassing the highly variable geographical features for the valley and agreeing well with the 9.1-μm data (Fig. 6, plus and open inverted triangle) bounded by the curves of $0.002\ sr^{-1} < \rho_{EHT} < 0.03\ sr^{-1}$. Another example[1] of ρ_{EHT} at 10.6 μm over the Coastal Range Mountains in California north of San Francisco ranged from 0.0144 to 0.0278 sr^{-1}. This example compares well with the 9.1-μm data (cross) which would correspond to the average $\rho_{EHT} \sim 0.012\ sr^{-1}$ curve. In addition, the ρ_{EHT} at 10.6 μm over relatively calm ocean water was approximately measured to be $\sim(1.8 \pm 0.2) \times 10^{-7}\ s \cdot {}^{-1}$. Backscatter from water surface is more difficult to quantify, owing to the effect of surface disturbances and, in addition, its wavelength dependence is not well known. Even so, the 10.6-μm value over open ocean surface is closer to the value of $\sim 10^{-8}$ sr^{-1} for 9.1 μm for a smooth water surface rather than to the 10^{-4} sr^{-1} value of the perturbed water surface with bubbles. These examples show that Earth-surface signals can be monitored consistently

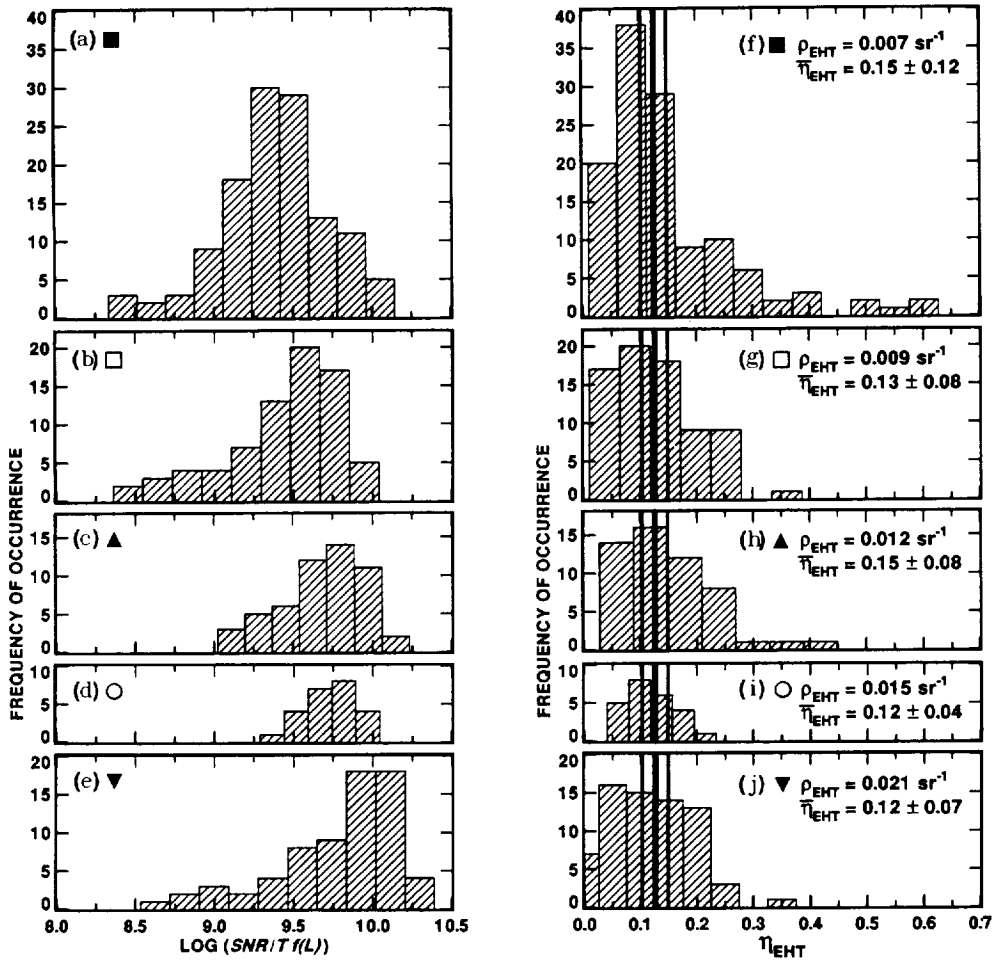

Fig. 7. Histograms of measured SNR normalized by the transmission efficiency T and $f(L)$ from the Earth's surface at various locations as shown in Fig. 5: (a) Coastal Range Mountains northeast of Santa Cruz, California (solid square); (b) agricultural land over Sacramento Valley near Willows, California (open square); (c) eastern slopes of the Sierra Nevada Mountains (filled triangle); (d) San Jose metropolitan area only at $L \sim 950$ m (open circle); and (e) Coastal Range Mountains east of Salinas, California (filled inverted triangle). Histograms of calculated lidar efficiency η_{EHT} from the respective Earth surfaces are shown in (f)–(j). The average ρ_{EHT} for each Earth-surface scenario as assessed from Fig. 6 is shown in the legend. The SND $\eta_{EHT} = 0.12 \pm 18\%$ for this mission is shown within the bold vertical lines for comparison with η_{EHT} from different Earth surfaces.

from different lidars and, therefore, may be used to calibrate the lidar in flight with *a priori* knowledge of the ρ_{EHT}.

4. Lidar Calibration from the Earth's Surface

The Earth surfaces sampled in flight were, for the most part, heterogeneous, and the SNR_{EHT} varied a fair amount. Figure 7(a)–7(e) histograms for five sets of data over different regions show the frequency of occurrence of measured SNR normalized by T and $f(L)$. These histograms give the distribution of range-independent SNR_{EHT}, which shows the variation, encountered during a roll, that is due to surface inhomogeneity only. Figure 7(a)–7(e) shows the position of the mode of distribution changing from lower- to higher-backscatter targets with the tightest distribution given for the metropolitan area in the South Bay area in Fig. 7(d), which suggests that it was the most uniform target with the least variability from each 1-s sample.

Homogeneous or even uniform heterogeneous targets [e.g., Fig. 7(d)] would be preferred for in-flight calibration, as they would give well-defined SNR_{EHT}, leading to well-defined lidar efficiency. However, since the Earth-surface targets sampled during the mission were mostly heterogeneous with varying SNR_{EHT}, any estimation of lidar efficiency η_{EHT} [with Eqs. (1)–(3)] from these data sets would also be associated with some variability. From the statistics of range-independent SNR_{EHT} shown in Fig. 7(a)–7(e), the statistics of η_{EHT} were determined with an average ρ_{EHT} corresponding to each of the five regions. These values for ρ_{EHT} of 0.007, 0.009, 0.012, 0.015, and 0.021 sr^{-1} were estimated for the curves that best fit the selected data samples shown in Fig. 6. The distributions of η_{EHT} are shown in Fig. 7(f)–7(j) with the mean η_{EHT} and its standard deviation for each distribution given in the legend. Figure 7(i), corresponding to the most uniformly distributed target, even though heterogeneous with the tightest distribution, gave mean

$\eta_{EHT} \sim 0.12$ with only 36% variation as compared with $\eta_{CHT} \sim 0.126$ with 18% uncertainty with CHT SND used during the mission, as stated in Subsection 3.B. The uncertainty in the η_{EHT} estimation here is dominated by the variability in the SNR_{EHT} from the complex heterogeneous surfaces. The most nonuniform Earth-surface target [Fig. 7(f)] gave mean $\eta_{EHT} \sim 0.15$ with a variation of ~80%, and if an appropriately varying ρ_{EHT} was known for such a target, then the estimation of η_{EHT} would be much less uncertain. These distributions show that if the Earth-surface backscatter is known then the lidar efficiency can be estimated with a fair degree of accuracy, preferably with uniform Earth-surface targets during flight for airborne or space-based lidar.

5. Conclusion

This paper characterizes the lidar backscatter of simulated Earth surfaces in the laboratory for their possible application as calibration targets for airborne and space-based lidars during flights. Several different simulated Earth surfaces were investigated, such as vegetation and nonvegetation land-type and wet-type surfaces. The land-type targets provide a fair envelope of Earth-surface backscatter for several materials. The backscatter of most dry Earth surfaces at various angles of incidence showed only weak to negligible angular dependence. The SNR data measured in the airborne MACAWS mission over various complex heterogeneous surfaces lie within the bounds of the values obtained in the laboratory. Thus data from different regions could be used for in-flight calibration to estimate the lidar efficiency and the associated uncertainty. The Earth-surface-derived lidar efficiency obtained with the average ρ_{EHT} of complex heterogeneous surfaces encountered during the mission gave good agreement with the CHT-derived lidar efficiency with least error associated with the most uniform target. Therefore, by measuring SNR_{EHT} from Earth surfaces with known ρ_{EHT}, using an airborne or space-based lidar, one can estimate the lidar system efficiency for atmospheric measurements. Obtaining absolute calibrated backscatter measurements with this method instead of signals in relative units has important advantages that lead to crucial information and immense research opportunities for various aspects of global aerosol modeling in terms of its impact on climate, pollution, and hydrological processes.

This research was partially supported under NASA subcontracts 95-193 and NCC8-142. The authors acknowledge the help of Amy Jai-Sien Lai, who was sponsored by NASA's Summer High School Apprenticeship Research Program and participated in the laboratory. The authors thank R. Kakar, Office of Earth Science, NASA Headquarters, for funding the cw lidar on the MACAWS mission, D. Chambers and J. Rothermel for mission support, and D. Cutten for providing the Earth-surface measurements from the 10.6-μm MACAWS pulsed lidar and attenuation factors from HITRAN and LOWTRAN 7.

References

1. J. Rothermel, D. R. Cutten, R. M. Hardesty, R. T. Menzies, J. N. Howell, S. C. Johnson, D. M. Tratt, L. D. Olivier, and R. M. Banta, "The multi-center airborne coherent atmospheric wind sensor, MACAWS," Bull. Am. Meteorol. Soc. **79,** 581–599 (1998).
2. M. A. Jarzembski, V. Srivastava, E. W. McCaul, Jr., G. J. Jedlovec, R. J. Atkinson, R. F. Pueschel, and D. R. Cutten, "Comparison of lidar backscatter with particle distribution and GOES-7 data in Hurricane Juliette," Geophys. Res. Lett. **24,** 1063–1066 (1997).
3. J. L. Spinhirne, S. Chudamani, J. F. Cavanaugh, and J. L. Bufton, "Aerosol and cloud backscatter at 1.06, 1.54, and 0.53 μm by airborne hard-target-calibrated Nd:YAG/methane Raman lidar," Appl. Opt. **36,** 3475–3490 (1997).
4. R. T. Menzies and D. M. Tratt, "Airborne CO_2 coherent lidar for measurements of atmospheric aerosol and cloud backscatter," Appl. Opt. **33,** 5698–5711 (1994).
5. Y. J. Kaufman and B. N. Holben, "Calibration of the AVHRR visible and near-IR bands by atmospheric scattering, ocean glint and desert reflection," Int. J. Remote Sens. **14,** 21–52 (1993).
6. W. E. Baker, G. D. Emmitt, P. Robertson, R. M. Atlas, J. E. Molinari, D. A. Bowdle, J. Paegle, R. M. Hardesty, R. T. Menzies, T. N. Krishnamurti, R. A. Brown, M. J. Post, J. R. Anderson, A. C. Lorenc, T. L. Miller, and J. McElroy, "Lidar-measured winds from space: a key component for weather and climate prediction," Bull. Am. Meteorol. Soc. **76,** 869–888 (1995).
7. M. J. Kavaya, G. D. Spiers, E. S. Lobl, J. Rothermel, and V. W. Keller, "Direct global measurements of tropospheric winds employing a simplified coherent laser radar using fully scalable technology and technique," Proc. Soc. Photo-Opt. Instrum. Eng. **2214,** 237–249 (1994).
8. W. L. Wolfe and G. J. Zissis, *The Infrared Handbook* (1978), Chap. 3.
9. M. J. Post and R. E. Cupp, "Optimizing a pulsed Doppler lidar," Appl. Opt. **29,** 4145–4158 (1990).
10. C. M. Sonnenschein and F. A. Horrigan, "Signal-to-noise relationships for coaxial systems that heterodyne backscatter from the atmosphere," Appl. Opt. **10,** 1600–1604 (1971).
11. R. T. Menzies, M. J. Kavaya, P. H. Flamant, and D. A. Haner, "Atmospheric aerosol backscatter measurements using a tunable coherent CO_2 lidar," Appl. Opt. **23,** 2510–2517 (1984).
12. M. A. Jarzembski, V. Srivastava, and D. M. Chambers, "Lidar calibration technique using laboratory-generated aerosols," Appl. Opt. **35,** 2096–2108 (1996).
13. J. Rothermel, D. M. Chambers, M. A. Jarzembski, V. Srivastava, D. A. Bowdle, and W. D. Jones, "Signal processing and calibration of continuous-wave focused CO_2 Doppler lidars for atmospheric backscatter measurement," Appl. Opt. **35,** 2083–2095 (1995).
14. M. J. Kavaya, R. T. Menzies, D. A. Haner, U. P. Oppenheim, and P. H. Flamant, "Target reflectance measurements for calibration of lidar atmospheric backscatter data," Appl. Opt. **20,** 2619–2628 (1983).
15. M. J. Kavaya, "The JPL lidar target calibration facility," in Digest of Third Topical Meeting on Coherent Laser Radar: Technology and Applications (Optical Society of America, Washington, D.C., 1985), p. II.1.
16. L. S. Rothman, R. R. Gamache, A. Goldman, L. R. Brown, R. A. Toth, H. M. Pickett, R. L. Poynter, J.-M. Flaud, C. Camy-Peyret, A. Barbe, N. Husson, C. P. Rinsland, and M. H. Smith, "HITRAN database: 1986 edition," Appl. Opt. **26,** 4058–4097 (1987).
17. F. X. Kneizys, E. P. Shettle, G. P. Anderson, L. W. Abreu, J. H. Chetwynd, J. E. A. Selby, S. A. Clough, and W. O. Gallery, "Atmospheric transmittance/radiance-computer code LOWTRAN 7," Report AFGL-TR-88-0177 (Air Force Geophysics Laboratory, Hanscom Air Force Base, Mass., 1988).